Biosensors and Bioelectronics 141 (2019) 111331

Contents lists available at ScienceDirect

Biosensors and Bioelectronics

journal homepage: www.elsevier.com/locate/bios

# In-situ growth of $NiWO_4$ saw-blade-like nanostructures and their application in photo-electrochemical (PEC) immunosensor system designed for the detection of neuron-specific enolase

Razium Ali Soomro[a,b,c,*], Nazar Hussain Kalwar[d], Ahmet Avci[e], Erol Pehlivan[f], Keith Richard Hallam[c], Magnus Willander[g]

[a] National Centre of Excellence in Analytical Chemistry, University of Sindh, Jamshoro, 76080, Pakistan
[b] Beijing Advanced Innovation Centre for Soft Matter Science and Engineering, Beijing University of Chemical Technology, Beijing, 100029, China
[c] Interface Analysis Centre, School of Physics, University of Bristol, Bristol, BS8 1TL, UK
[d] Institute of Chemistry, Shah Abdul Latif University Khairpur, 66020, Pakistan
[e] Department of Mechanical Engineering, Faculty of Engineering, University of Selcuk, Campus, 42079, Konya, Turkey
[f] Department of Chemical Engineering, Faculty of Engineering, University of Selcuk, Campus, 42079, Konya, Turkey
[g] Department of Science and Technology, Campus Norrkoping, Linkoping University, SE-60174, Norrkoping, Sweden

ARTICLE INFO

*Keywords:*
$NiWO_4$ nanostructures
Neuron-specific enolase
Indium tin oxide electrode
Biosensor

ABSTRACT

This study describes the construction of highly-sensitive photo-electrochemical (PEC) immunosensor for the detection of neuron-specific enolase (NSE). The biosensing platform is comprised of photo-active $NiWO_4$ nanostructures, in-situ-grown over a conductive substrate (indium tin oxide) using a low-temperature template-based co-precipitation approach. The discussed approach enables the formation of discrete, yet morphologically-analogous, nanostructures with complete coverage (pinhole-free) of the electrode surface. The in-situ-grown nanostructure possess dense population with sharp saw-blade like morphological features that can support substantial immobilisation of anti-NSE agent. The constructed platform demonstrated excellent photo-catalytic activity towards uric acid (UA) which served as the base for the Electrochemical –mechanism (EC) based PEC inhibition sensing. The detection of NSE, relied on its obstruction in analytical signal observed for the photo-oxidation of UA after binding to the electrode surface via protein-antibody interaction. The constructed PEC immunosensor exhibits signal sensitivity up to 0.12 ng $mL^{-1}$ of NSE with excellent signal reproducibility and electrode replicability. Moreover, the constructed platform was successfully used for NSE determination in human serum samples.

## 1. Introduction

The synergic combination of photo-excitation and electrochemical detection has caused PEC to be described as an adaptable technique, capable of detecting diverse biological and chemical entities (Britto et al., 1996; Zhang et al., 2019). The simple operation protocols and affordable cost, with separate excitation (light) and detection signal sources, makes PEC an ideal contender for biosensing application (Gutiérrez et al., 2017; Yu et al., 2019). Since, PEC's performance is based on charge transfer between the analyte and photo-catalytic material upon light irradiation, the choice of photo-catalytic material and electrode engineering plays a key role in determining the sensitivity of the system (Atchudan et al., 2019; Wang et al., 2019). In particular, PEC platforms designed for bio-recognition purposes require matrix materials with large surface area and sufficient photo-activity for immobilisation of the recognition element and production of measurable readout signals. To date, numerous materials, including metal-organic frameworks, graphitic carbon nitride ($g\text{-}C_3N_4$), transition metal dichalcogenide and semi-conductors, have been proposed to achieve superior PEC performance, based on their large accessible surface area and ordered crystallinity that are known to improve the photo-activity and restrict charge-carrier recombination (Li et al., 2019; Niu et al., 2013; Xu et al., 2015). Nanostructures possessing hierarchical structures, complex shapes and unique morphologies have shown more promising photo-activity compared to conventional counterparts (Hao et al., 2018). Heterojunctions of metal oxides with diverse materials, including conductive polymers and carbonaceous materials of various natures, are considered promising (Liu et al., 2019; Pang et al., 2018;

* Corresponding author. National Center of Excellence in Analytical Chemistry, University of Sindh, Jamshoro, 76080, Pakistan.
*E-mail address:* raziumsoomro@gmail.com (R.A. Soomro).

https://doi.org/10.1016/j.bios.2019.111331
Received 12 February 2019; Received in revised form 14 May 2019; Accepted 15 May 2019
Available online 08 June 2019
0956-5663/ 

Soomro et al., 2017; Tunesi et al., 2016; Wu et al., 2018). The need for an efficient immobilisation matrix is another strict requirement when it comes to designing PEC biosensors, particularly for clinical purposes. To achieve this, complex combinations of 3D polymeric nanosponges supported over graphene-incorporated 2D $TiO_2$ nanowires and synergic combination of $TiO_2$ nanorod arrays and $\alpha$-$Fe_2O_3$ shells have been reported (Hasanzadeh et al., 2017; Soomro, 2017). Although promising, such combinations are often limited by their high synthesis cost, associated toxicity and procedural complexity, which do not suffice for the desired characteristics that are needed to develop a single platform capable of PEC sensing of clinically-important molecules. Thus, the development of a single platform that possesses high photo-catalytic activity and comprises nanostructures possessing structural features/morphology that could support greater immobilisation is highly challenging.

In the context of photo-activity, tungstate-based nanomaterials have gained significant research attention due to their high surface area and suitable yet tuneable band gap positions (Barton et al., 2015). Among many, the monoclinic wolframite structure-based nickel tungsten oxide ($NiWO_4$) has some impressive characteristics, such as high structural stability, high conductivity and potential electrochemical properties (Kalwar et al., 2017). Literature supports the application of $NiWO_4$-based systems for PEC water oxidation and photo-catalytic application, where the performance the $NiWO_4$-based platforms has been shown to be better than that of $TiO_2$ (Tunesi et al. 2017, 2018). However, the use of such material in developing PEC platforms for biosensing application is still at an early stage due to the difficulty in obtaining a designed morphology with suitability for greater immobilisation. In addition to this, the integration of such nanostructures in an electrode system designed for PEC measurement using the conventional approach (drop-casting) suffers the complication of non-uniform deposition and structural stacking (Tunesi et al., 2017). These complications, including interfacial pinhole formation, negatively affect the overall performance of current-generation PEC biosensors. To overcome such issues, in-situ growth of 2D $NiWO_4$ nanostructures over conductive substrates, such as indium tin oxide (ITO), can be a viable option. However, one of the major obstacles to achieve in-situ growth is the direction and control of the growth process to obtain uniform and ordered 2D nanostructure layers. Thus, an efficient synthesis strategy that would allow for directional growth of photo-active materials over conductive substrates is another challenge, besides designing appropriate morphologies for immobilisation in PEC biosensor systems.

Unlike electrochemical biosensors, PEC immunosensors integrate the inherent sensitivity of PEC and selectivity for specific interaction (Zhu et al., 2018). In particular, label-free PEC immunosensors based on photo-electroactive materials capable of producing measurable readout signals and greater immobilisation area could drastically enhance PEC biosensor sensitivity, particularly for low-concentration clinical analysis. In this context, rapid and sensitive detection of biomarkers such as neuron-specific enolase (NSE) has high clinical advantages for early stage diagnosis, assessment of disease progression and therapeutic treatment efficacy, which could contribute to the long term survival of cancer patients (Muoio et al., 2018). Conventional techniques commonly used for detection of NSE include enzyme-linked immunosorbent assay (Berg et al., 2015; Liu et al., 2018a), radio immunoassay (Pussard et al., 2014) and fluorescence immunoassay (Song et al., 2015). However, such techniques, despite their measurement precision, suffer from disadvantages like complex sample preparation protocols, expensive maintenance and the need for proper infrastructure. On the contrary, PEC biosensor systems offer advantages like ease of operation, needlessness of infrastructure and inexpensive maintenance, together with the possibility of miniaturisation and field applicability (Wang et al., 2016).

In this study, we report the development of a highly-sensitive PEC immuno-biosensor system designed for the detection of NSE. The designed PEC system is based on highly photo-electroactive $NiWO_4$ nanostructures, grown directly (in-situ) over a conductive substrate (ITO) using a template-controlled low-temperature co-precipitation approach. This synthesis strategy allows the formation of highly ordered and uniform photo-active $NiWO_4$ nanostructures, over ITO, with morphologies that possess substantial immobilisation capacity for anti-NSE. The 2D $NiWO_4$ nanostructures with improved photo-activity and interface characteristics demonstrate excellent photo-catalytic activity against uric acid (UA), which served as a mediator for this EC-mechanism-based detection approach. The subsequent obstruction in the PEC oxidation signal of UA, with the addition of NSE over the surface of the photo-electrode previously immobilised with anti-NSE, was considered a primary signal response. The EC-mechanism-based signal inhibition approach enabled sensitive detection of NSE, with PEC signal sensitivity measurable up to 0.12 ng $mL^{-1}$. Moreover, the developed platform demonstrated excellent practical workability when tested for NSE determination from human serum samples.

## 2. Materials and methods

All the chemicals considered were analytical grade. Precursor salts, including nickel chloride hexahydrate ($NiCl_2{\cdot}6H_2O$) and sodium tungstate dihydrate ($Na_2WO_4{\cdot}2H_2O$), were obtained from Merck. Hydrazine hydrate ($N_2H_4{\cdot}H_2O$) (60%) was purchased from Sigma-Aldrich (Germany). The solvents, such as hydrochloric acid (HCl), sodium hydroxide (NaOH) and phosphate-buffered saline (PBS; pH 7.0), were purchased from Thermo Fisher Scientific. 3-[(3-cholamidopropyl)dimethylammonio]-1-propanesulfonate (CHAPS), UA ($C_5H_4N_4O_3$), ascorbic acid (AA; $C_6H_8O_6$), dopamine (DP; $C_8H_{11}NO_2$) and 6 mercapto-1-hexanol (MCH) were obtained from Sigma. The NSE protein and anti-NSE were purchased from Abcam (Cambridge, UK).

### 2.1. Instrumentation

Insights into the morphology and interface of the developed photo-electrode were obtained from field emission scanning electron microscopy (FE-SEM) analysis (Zeiss Sigma) equipped with an energy-dispersive x-ray spectroscopy (EDS) detector. Compositional purity was assessed using x-ray diffraction (XRD; Bruker D-8) and x-ray photo-electron spectroscopy (XPS; Scienta ESCA200). Phase analysis was performed using Raman spectroscopy (WITech alpha300). Optical measurements were carried using an UV–Vis spectrophotometer (Shimadzu). An electrochemiluminescence immunoassay analyser (Roche Cobas E601; Germany) was used to validate the detection of NSE from human serum samples. Electrochemical experiments were performed using an electrochemical workstation (Shanghai Chenhua Apparatus CHI830C; China) equipped with a PLS-SXE 300 xenon lamp as the light source for PEC measurements. The distance between the light source and photo-cell was maintained at 10 cm. The analysis was carried out in a typical three-electrode cell with the developed photo-electrode as the working electrode, platinum wire as the auxiliary and saturated calomel as the reference. Electrochemical impedance spectroscopy (EIS) measurements were recorded using $K_4Fe(CN)_6/K_3Fe(CN)_6$ (5 mM) as redox probe with frequency range of 100 kHz - 0.01 Hz and constant voltage of 0.2 V. The photo-current density versus time measurements were carried out at a constant voltage of +0.3 V in reference to Ag/AgCl electrode with 1.5 mM UA in 0.1 M PBS (pH 7.0). Photo-cycles were recorded for 150 s, with 20 s light on/off intervals.

### 2.2. In-situ growth of $NiWO_4$ over ITO substrate

In-situ growth of $NiWO_4$ nanostructures over ITO electrode was achieved using template-based co-precipitation. In a typical procedure, 0.075 g of $Ni(NO_3)_2{\cdot}6H_2O$ was allowed to homogenise in 20 ml of de-ionised water maintained at 50 °C. 0.086 g of $Na_2WO_4{\cdot}2H_2O$ was then introduced into the solution, drop-wise, followed by continuous stirring to achieve complete homogenisation. 0.7 g of CHAPS was then added as

the template. Once a clear solution was attained, pre-cleaned ITO substrate was introduced, with the conductive side facing outwards (Fig. S1). Nucleation was initiated by adding 120 µL of $N_2H_4{\cdot}H_2O$ slowly down the side of the container, where a change in colour from clear to sky blue indicated the start of the reaction. The reaction time was set to 3 h. Thereafter, the immersed ITO was slowly removed from the container and gently washing with a stream of de-ionised water to remove excessive loosely-bound template molecules. The ITO substrates were then subjected to calcination at 400 °C in a box furnace to complete the growth of $NiWO_4$ nanostructures. This electrode is designated as ITO/$NiWO_4$.

### 2.3. Immobilisation of anti-NSE agent

To induce immunosensing characteristics, the ITO/$NiWO_4$ was treated with anti-NSE agent (5 µg $mL^{-1}$) for 24 h of maturation time while maintained at 4 °C. The electrode was then washed with PBS (pH 7.0) to remove unbound antibodies, followed by treatment with 1.3 mM of the MCH blocking agent for at least 45 min to cover non-specific active sites of the photo-active electrode. The electrode was then stored at 4 °C, and is designated as ITO/$NiWO_4$/Ab throughout the manuscript for better readability. The immobilisation steps and their effect on the electro-catalytic activity of the developed immunosensor are generalised in Figure S2.

## 3. Results and discussion

### 3.1. Characterisation of photo-electrode (ITO/$NiWO_4$)

Morphological evaluation of the photo-electrode was carried using FE-SEM. Fig. 1 shows typical SEM images captured at different magnifications and viewpoints. A dense distribution of nanostructures with uniform structural features and negligible structural collapse is evident. The formation of saw-blade-like structural features is evident. The average thickness of the associated tooth is estimated to be in the range of 20–40 nm. More importantly, the cross-sectional view of the photo-electrode (Fig. 1e) is indicative of a pinhole-free surface coverage of nanostructures. Such coverage supports a compact interface comprising a high number of grain interfaces and conductive pathways that would significantly improve sensitivity of the PEC biosensor. The SEM image for an ITO electrode fabricated without the assistance of a template is shown as Figure S3. As seen, the formed material is without any structural features or specific morphology, which indicates the crucial role of the template (CHAPS) in obtaining the discussed morphology.

Fig. 1f shows the result of EDS mapping the $NiWO_4$ nanostructures. The presence of all three elements, W, Ni and O, in the nanostructures indicates the composition purity of the synthesised product. Although morphology-dependent electrochemical systems, particularly based on $NiWO_4$, have been reported previously for various nanostructures, including nanoberries and nanoflowers (Bahner et al., 2018; Huang et al., 2017), these have failed to allow controlled or slow growth of $NiWO_4$ nanostructures and, thus, have required rudimentary drop-casting of the nanostructures over the electrode surface. This is not amenable to production of sensor devices for point-of-care (POC) diagnostics. In contrast, the proposed method is based on in-situ growth of photo-active $NiWO_4$ over a conductive substrate, i.e. ITO, and can enable production of portable photo-electrodes with electrochemical characteristics that could be promising in constructing POC devices. Figure S4 shows an XRD pattern recorded for the as-synthesised $NiWO_4$ nanostructures. The pattern consists of peaks assigned to the (011), (110), (111), (021), (200), (102), (112), (211), (022), (220), (130), (221), (113), (023) and (041) planes of the wolframite monoclinic structure of $NiWO_4$, as referenced against ICCD card 01-072-1189.

XPS analysis further confirmed the elemental composition of the $NiWO_4$ nanostructures. The complete survey spectrum shown in Fig. 2a consists of peaks attributed to nickel, tungsten and oxygen. The presence of surface-bound extraneous carbon is also evident. The higher-resolution spectrum recorded for Ni $2p_{3/2}$ and Ni $2p_{1/2}$ consist of peaks at 855.7 and 873.4 eV, respectively, with satellite peaks established at 862.4 and 879.7 eV (Fig. 2b). The difference in binding energy (17.7 eV) between the two peaks of Ni $2p_{3/2}$ and Ni $2p_{1/2}$ confirmed the divalent oxidation state of Ni atoms present in $NiWO_4$ nanostructures. The O 1s binding energy was measured at 532.5 eV (Fig. 2c), while the W $4f_{7/2}$ and W $4f_{5/2}$ binding energies were noted at 35.02 and 36.9 eV, reflecting a $W^{6+}$ oxidation state (Fig. 2d). The observed binding energies are in complete agreement to those reported for pure $NiWO_4$ material (Huang et al., 2017).

Raman spectroscopy was used for phase analysis. Figure S5 presents the Raman spectrum for as-synthesised $NiWO_4$, with characteristic bands measured at 889, 769, 694, 545, 509 and 418 $cm^{-1}$. The observed peaks are in complete agreement with other related studies (Bahner et al., 2018). The high intensity Raman band observed at 889 $cm^{-1}$ is attributed to W–O bond stretching whereas 769 $cm^{-1}$ could be assigned to O–W–O, further confirming the wolframite ($WO_4$) nature of the synthesised nanostructure.

Optical characteristics of the as-synthesised photo-active material were also assessed. Figure S6 shows the UV–Vis absorption spectra of the material recorded in the range of 400–800 nm. The material

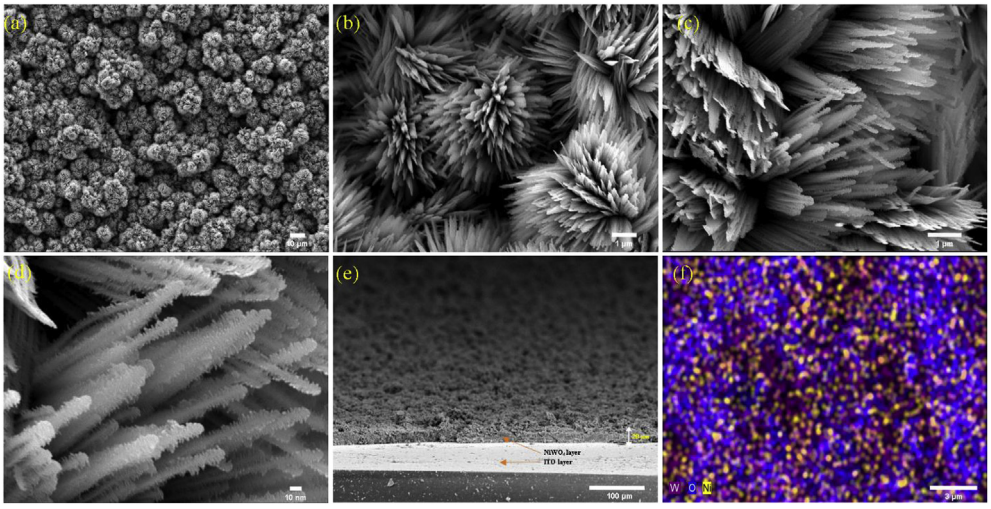


**Fig. 1.** (a-d) FE-SEM images captured for ITO/$NiWO_4$ at various magnifications. (e) Cross-section of ITO electrode with in-situ-grown layer of $NiWO_4$ nanostructure, and (f) EDS elemental mapping indicating presence of Ni, W and O.

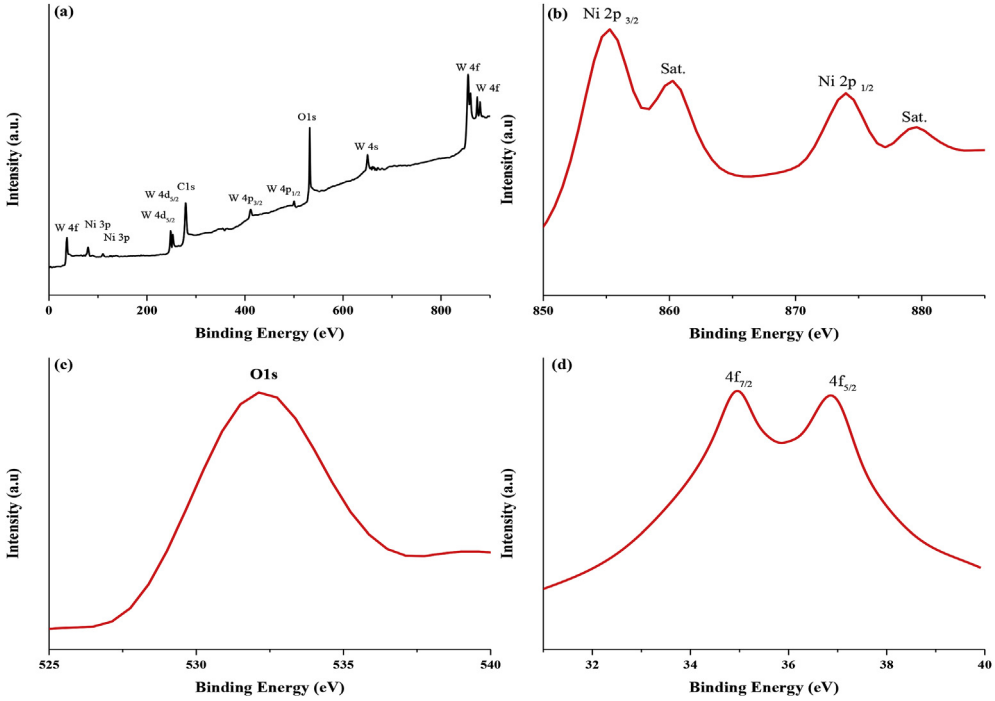


**Fig. 2.** XPS analysis of in-situ-grown $NiWO_4$ nanostructures. (a) Survey spectrum consisting of peaks assigned to Ni, W and O. (b-d) High-resolution spectra for Ni2p, O1s and W4f binding energy regions, respectively.

exhibits three absorption edges, between 400 and 750 nm. Such characteristics are linked to the material's capability to act as a light absorber (Ilkhani et al., 2016). The band-gap, from the corresponded Tauc plot (inset Figure S6), was estimated to be 2.05 eV, which is close to the value reported for the $NiWO_4/WO_3$ heterojunction system and $NiWO_4$ nano-barriers used in photo-catalytic applications (Bahner et al., 2018; Huang et al., 2017). In this case, the smaller band-gap can support faster electron mobility that could improve the sensitivity of the PEC biosensor.

### 3.2. Electrochemical characteristics of ITO/$NiWO_4$

Cyclic voltammetry (CV) is one of the basic techniques used for the electrochemical characterisation of developed electrodes. The electrochemical behaviour of the ITO/$NiWO_4$ was evaluated before immobilisation of anti-bodies (anti-NSE) in 0.1 M PBS (pH 7.0) at a fixed scan rate of 50 mV $s^{-1}$. Fig. 3 shows the CV profile with a pair of redox peaks at 0.44 and 0.27 V. This pair is attributed to the redox couple of nickel ($Ni^{2+}/Ni^{3+}$) associated with $NiWO_4$ (Rubianes and Rivas, 2003). Similar redox couples with slightly positive-shifted potential values have been reported for various $NiWO_4$ nanostructures that have been considered for photo-catalytic application (Huang et al., 2017). The observed redox potential in this case is negatively-shifted in addition to high current density compared to the template-free counterparts (Fig. 3a). This variation in current density and potential value between the two similar materials is a direct consequence of morphology, uniform distribution of nanostructures and complete interfacial contact between modifier and electrode surface. Fig. 3b, depicts the variation in the anodic and cathodic response of ITO/$NiWO_4$ with increasing scan rate in range from 50 to 100 mV $s^{-1}$. As seen, the redox peaks at high scan rates have maintained their peak shapes, which indicate an electrochemically reversible electron transfer process of the diffusing redox species. The corresponding anodic and cathodic peak current were then plotted against the square root of scan rate. The observed linear trend shown in the inset of Fig. 3b, further confirms the $Ni^{2+}/Ni^{3+}$ redox process to be diffusion controlled (Elgrishi et al., 2018).

Since NSE detection is based on an EC mechanism, the photo-catalytic activity of ITO/$NiWO_4$ was also studied against suitably-oxidisable molecules, including AA, UA and DP. Fig. 4 shows the CV responses recorded for ITO/$NiWO_4$ against 1.5 mM solutions of each biomolecule under no-illumination conditions. The major peaks observed at 0.68, 0.47 and 0.30 V were attributed to oxidation of DP, AA and UA, respectively. Judging from the high current density and low over-potential value of peak III, it is evident that ITO/$NiWO_4$ exhibits relatively superior electro-catalytic activity towards UA compared to the other competitive molecules. To understand the effect of co-existing molecules on the oxidation of UA, the electro-catalytic oxidation was carried in the presence of AA, DP, glucose, and urea. To ensure high signal sensitivity and minimum peak overlapping, differential pulse voltammetry (DPV) was performed in a potential window of 0.2–0.8 V with concentration of each component set to 1.5 mM. As observed, (Figure S7), the ITO/$NiWO_4$ was capable of oxidising these molecules, however relatively low oxidation potential with high current signal output was achieved in case of UA compared to other competing molecules. Thus, it's safe to establish that presence of other co-existing molecules would have negligible effect on the electro-catalytic oxidation of UA occurring at the surface of ITO/$NiWO_4$.

The photo-electrocatalytic behaviour of ITO/$NiWO_4$ was studied under illumination conditions. For an optimum response, the concentration of UA and illumination wavelength were optimized. Figure S8 (a) shows the variation of photocurrent response against different concentrations of UA in range of 0.5–2.0 mM. As seen, the photo-response measured for 1.5 mM UA, endures the highest photocurrent, thereafter declining with slight shift in the noted oxidation potential value. Figure S8 (b) depicts the variation in measured photo-current against different illumination wavelengths. A gradual increase in the measured photo-current is evident in range of 580–600 nm. The maximum photo-current was measured near 600 nm which then decreases rapidly beyond 610 nm. This abrupt decline could be ascribed to the inability of low-frequency photons to achieve abundant charge carrier excitation in the as-synthesised small bandgap $NiWO_4$ nanostructures. Under the optimum conditions, the overall the current response of ITO/$NiWO_4$ was noted to increase by a factor of 1.44 (Fig. 4b). This increase in the generated photo-current can be explained via the photo-active EC

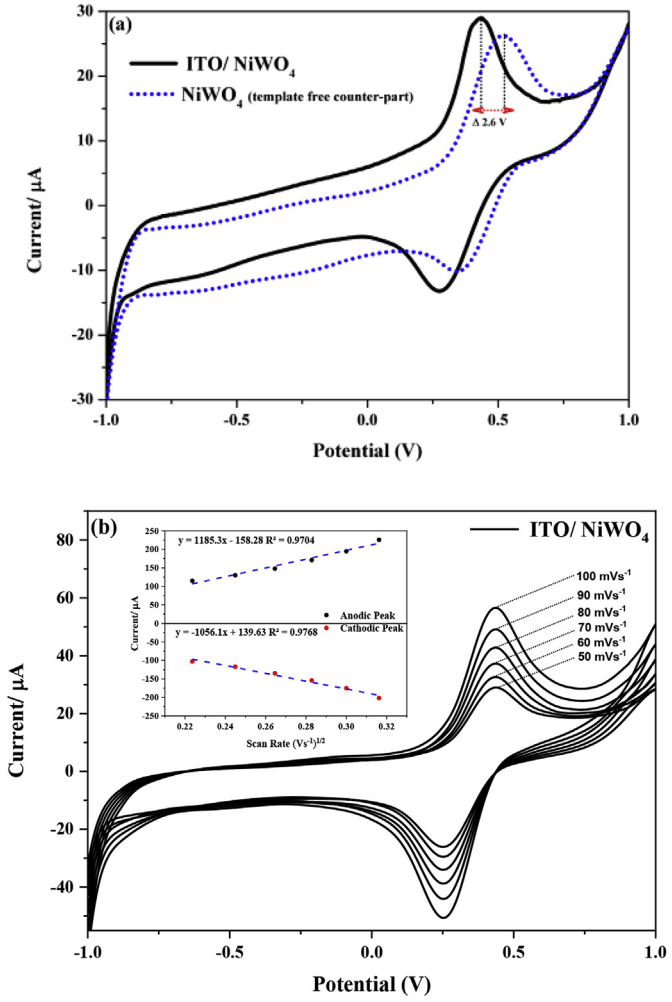


**Fig. 3.** (a) CV behaviour of ITO/$NiWO_4$ in reference to its template-free counterpart deposited on GCE at a fixed scan rate of 50 mV.s-1. (b) Increasing anodic and cathodic responses of ITO/NiWO4 against gradual rise of scan rate from 50 to 100 mV.s-1. (inset) Graph justifying the observed linearity between current and square root of scan rate.

mechanism. It has been established that electron donors can significantly scavenge photo-generated holes, thereby inhibiting charge-carrier recombination and, therefore, increasing the photo-current (Si and Song, 2018). Here, in the presence of UA, when the electrode is exposed to light, photo-generated electrons from the conduction band of the $NiWO_4$ nanostructure tend to transfer to the ITO electrode. UA acts as an electron donor, oxidising and blocking the charge-carrier recombination process by contributing to electron promotion from the conduction band of $NiWO_4$ to the ITO electrodes (Figure S9). These electrons are, thus, responsible for the enhanced photo-current observed for UA under illumination. From these results, it was confirmed that the PEC oxidation of UA is a favourable process at the surface of ITO/$NiWO_4$, and that UA can serve as a mediator/facilitator in the photo-active EC mechanism designed for detection of NSE biomarker.

### 3.3. Construction of PEC immunosensor

To induce immuno-selectivity in the developed electrode, the ITO/$NiWO_4$ was treated with anti-NSE agent, as described in Section 2.3. The CV profile shown in Figure S10a for the photo-catalytic oxidation of UA is suggestive of declined current response for ITO/$NiWO_4$/Ab compared to ITO/$NiWO_4$. This decline is a consequence of fewer active sites available for photo-electrocatalytic oxidation of UA subsequent to the immobilised proteins. It is known that electrode-transfer resistance is a function of insulating features on the surface or interface of the electrode. Thus, the diameter of the semi-circular section of the Nyquist plot obtained by EIS measurement can provide crucial information about the electrode modification process. Figure S10b shows the Nyquist plot for ITO/$NiWO_4$ and ITO/$NiWO_4$/Ab under constant illumination conditions against 4.0 mM $K_4Fe(CN)_6/K_3Fe(CN)_6$ in PBS (pH 7.0). The Nyquist plot recorded for ITO/$NiWO_4$ exhibits a relatively smaller diameter compared to that observed for ITO/$NiWO_4$/Ab. The increased charge transfer resistance (larger semi-circle) in the case of ITO/$NiWO_4$/Ab further points to the successful immobilisation of anti-NSE agent over the surface of photo-electrode. The photo-current responses versus time for ITO/$NiWO_4$ and ITO/$NiWO_4$/Ab, in reference to bare ITO, were also recorded (Figure S10c). The measurements were carried out with 20 s light on/off cycles for about 150 s. When the electrode was under illumination, the current recorded on ITO/$NiWO_4$ rapidly rose from 0.65 to 185 µA. The observed photo-current was noted to increase rapidly under illumination and then remain consistent throughout the period. By contrast, the bare ITO electrode exhibited negligible response. The ITO/$NiWO_4$/Ab, when subject to illumination, produced slightly-decreased photo-current (163 µA) compared to ITO/$NiWO_4$. This slightly-decreased photo-current was a consequence of the insulating behaviour of the anti-bodies immobilised over the surface of the electrode that attenuates the electron transfer process between UA and ITO electrode, thus ensuring successful immobilisation and construction of PEC immunosensors. It should be emphasised here that the photo-response observed is relatively greater than that noted for other nanostructures (Bahner et al., 2018; Huang et al., 2017; Si and Song, 2018; Yin et al., 2017). The high-throughput response of ITO/$NiWO_4$ is basically a synergic outcome of the favourable band-gap (2.09 eV), in-situ-grown uniform layer of $NiWO_4$ and saw-blade-like morphological features of $NiWO_4$ nanostructures. Such a combination induces efficient light absorption and charge-separation characteristics to enhance PEC activity, which is a consequence of nano-size structural features with

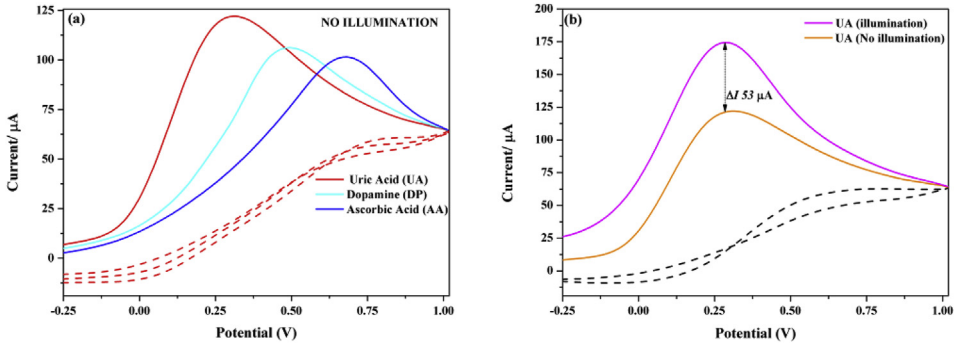


**Fig. 4.** (a) CV curves depicting oxidation of UA, DP and AA with equimolar concentration of 1.5 mM under no-illumination condition (b) increased photocurrent oxidation response for UA under the illumination condition using ITO/$NiWO_4$ as working electrode respectively.

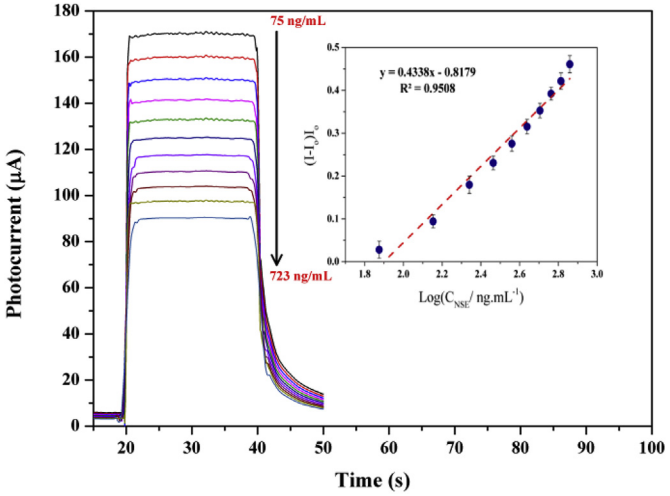


**Fig. 5.** Photocurrent responses of ITO/$NiWO_4$/Ab against different concentrations of NSE ranging from 75 to 723 ng.mL-1. (inset) Corresponded calibration curve plotted between photocurrent and log of NSE concentration. Measurements were carried out in 0.1 M PBS (pH 7.0) with 1.5 mM UA at a bias potential of +0.3 V.

greater exposure area and more active sites for PEC reaction (Hasanzadeh et al., 2017).

### 3.4. Analytical performance of PEC immunosensor

Under optimum conditions, the analytical performance of the developed PEC immunosensor was studied against different concentration NSE standards. The measurements were obtained under constant light conditions, with 0.1 M PBS (pH = 7.0) containing 1.5 mM UA. Since NSE detection is based on inhibiting the photo-active response of UA, a gradual decrement in the photo current response proportional to the concentration of NSE was expected as a consequence of the formation of an immunocomplex between anti-NSE and NSE antigen. Thus, the difference in photo-current before and after incubation of each specific concentration of NSE was considered to be the quantitative PEC signal. Fig. 5 shows the calibration of photo-current $((I–I_0)/I_0)$ obtained against log concentration of NSE. The photo-response of the developed PEC sensor was noted to exhibit good linearity in the range of 75–723 ng $mL^{-1}$ (inset of Fig. 5). The detection limit (3x S/N) was estimated to be 0.12 ng $mL^{-1}$ of NSE. Table 1 compares the analytical performance of the sensor with various other sensor systems.

### 3.5. Selectivity and reproducibility of the developed PEC immunosensor

The variation in the photo-response of ITO/$NiWO_4$/Ab was measured against common co-existing antigens, such as prostate-specific antigen and carcinoembryonic antigen under similar conditions as those in Section 3.4. The developed photo-electrode (ITO/$NiWO_4$/Ab) was incubated separately with NSE (75 ng $mL^{-1}$) and NSE plus interferent solutions. The corresponded variation in photo-current is given in Figure S11a. The negligible variation in the photo-current in the presence of biomolecules other than NSE signifies the immunoselective response of the biosensor. The reproducibility of the electrode was assessed separately by fabricating five electrodes (ITO/$NiWO_4$/Ab) using the sample procedure described in Section 3.3. The photo-current for the devised electrode, was measured under constant illumination conditions against 75 ng $mL^{-1}$ of NSE in the presence of 0.1 M PBS (pH 7.0) containing 1.5 mM of UA. The variation in photo-current for the corresponding electrodes is presented in Figure S11b. The electrodes exhibited similar photo-responses, with minimum variation in the measured photo-current. The observed signal reproducibility is crucial for standard measurements and, in this case, the in-situ-grown $NiWO_4$ nanostructures provide identical interfaces for in-coming biomolecules and, thus, we anticipate signal reproducibility each time a similar electrode is fabricated.

### 3.6. Application of developed PEC immunosensor for clinical analysis

The immunosensor was tested in real clinical serum specimens obtained from volunteers, with their written consent. A total of five specimens were analysed using the proposed PEC immunosensor without any sample pre-treatment, and their results were compared with those obtained using a standard electrochemiluminescent method (Yu et al., 2012). Table S2 compares the values obtained from the two methods. It is clear that the relative standard deviation observed for the measurements of the proposed sensor is within acceptable limits and, thus, the proposed sensor could be used for clinical analysis. Since no sample pre-treatment was carried out before analysis, it is safe to assume that matrix interference towards the developed PEC immunosensor is negligible.

## 4. Conclusions

In this study, we report the development of a PEC platform designed to detect NSE biomarker. The platform comprises of highly versatile saw-blade-like $NiWO_4$ nanostructures, grown in-situ over ITO electrode using simple co-precipitation approach. Here, the quantification of NSE was achieved by EC-mechanism, where the obstruction in PEC oxidation of UA subsequent to protein-antibody interaction was taken as the primary signal. The developed approach enabled highly sensitive detection of NSE biomarker within the analytical range of 723 to 75 ng/ml with signal sensitivity measurable up to 0.12 ng $mL^{-1}$. The proposed PEC sensor was capable of analysing clinical specimens consisting of NSE which reflected its practicality to be engineered for other clinically-important biomolecules. Although, the devised platform possess excellent PEC characteristics, achieving high signal sensitivity without compromising the interface integrity and signal stability is still a major challenge. To overcome such issues, research focus must be directed towards designing superior combinations of photoactive materials with potential to be used in portable point-of-care devices.

## Declaration of interests

The authors declare that they have no known competing financial

**Table 1**
Analytical characteristics of the proposed sensor in comparison to other related sensor systems designed for sensitive detection of NSE biomarker.

| Fabricated electrode | Technique | Linear working range (ng.$mL^{-1}$) | Limit of detection (ng.$mL^{-1}$) | Reference |
|---|---|---|---|---|
| HRP-P4/anti-P4/GCE | Microfluidic immunosensor | 0.50–12.5 | 0.20 | Arévalo et al. (2010) |
| HRP-anti-AFP/AFP/anti-AFP/AuNPs/CPE | Electrochemical immunosensor | 0.50–80 | 0.25 | Ding et al. (2009) |
| FITC-anti-IgM/IgM/anti-IgM/eggshell membrane | Fluorescence immunosensor | 5–60 | 4.30 | Tang et al. (2011) |
| CEA/anti-CEA/CNTs-AuNPs/GCE | Electrochemical immunosensor | 0.10–200 | 0.04 | Gao et al. (2011) |
| PPD-GR nanocomposite | Electrochemical immunosensor | 1–1000 | 0.3 | Amani et al. (2018) |
| ITO/$NiWO_4$/Ab | PEC immunosensor | 75–723 | 0.12 | **This work** |

interests or personal relationships that could have appeared to influence the work reported in this paper.

## CRediT authorship contribution statement

**Razium Ali Soomro:** Formal analysis, Investigation, Methodology. **Nazar Hussain Kalwar:** Conceptualization. **Ahmet Avci:** Supervision. **Erol Pehlivan:** Resources, Supervision. **Keith Richard Hallam:** Writing - review & editing. **Magnus Willander:** Supervision.

## Acknowledgments

The authors acknowledge the experimental support provided by NCEAC, Jamshoro, Pakistan.

## Appendix A. Supplementary data

Supplementary data related to this article can be found at https://doi.org/10.1016/j.bios.2019.111331.

## References

Amani, J., Maleki, M., Khoshroo, A., Sobhani-Nasab, A., Rahimi-Nasrabadi, M., 2018. An electrochemical immunosensor based on poly p-phenylenediamine and graphene nanocomposite for detection of neuron-specific enolase via electrochemically amplified detection. Anal. Biochem. 548, 53–59.

Arévalo, F.J., Messina, G.A., Molina, P.G., Zón, M.A., Raba, J., Fernández, H., 2010. Determination of progesterone (P4) from bovine serum samples using a microfluidic immunosensor system. Talanta 80 (5), 1986–1992.

Atchudan, R., Muthuchamy, N., Edison, T.N.J.I., Perumal, S., Vinodh, R., Park, K.H., Lee, Y.R., 2019. An ultrasensitive photoelectrochemical biosensor for glucose based on bio-derived nitrogen-doped carbon sheets wrapped titanium dioxide nanoparticles. Biosens. Bioelectron. 126, 160–169.

Bahner, N., Reich, P., Frense, D., Menger, M., Schieke, K., Beckmann, D., 2018. An aptamer-based biosensor for detection of doxorubicin by electrochemical impedance spectroscopy. Anal. Bioanal. Chem. 410 (5), 1453–1462.

Barton, L.E., Auffan, M., Olivi, L., Bottero, J.-Y., Wiesner, M.R., 2015. Heteroaggregation, transformation and fate of CeO 2 nanoparticles in wastewater treatment. Environ. Pollut. 203, 122–129.

Berg, B., Cortazar, B., Tseng, D., Ozkan, H., Feng, S., Wei, Q., Chan, R.Y.-L., Burbano, J., Farooqui, Q., Lewinski, M., Di Carlo, D., Garner, O.B., Ozcan, A., 2015. Cellphone-based hand-held microplate reader for point-of-care testing of enzyme-linked immunosorbent assays. ACS Nano 9 (8), 7857–7866.

Britto, P., Santhanam, K., Ajayan, P., 1996. Carbon nanotube electrode for oxidation of dopamine. Bioelectrochem. Bioenerg. 41 (1), 121–125.

Ding, C., Zhao, F., Ren, R., Lin, J.-M., 2009. An electrochemical biosensor for α-fetoprotein based on carbon paste electrode constructed of room temperature ionic liquid and gold nanoparticles. Talanta 78 (3), 1148–1154.

Elgrishi, N., Rountree, K.J., McCarthy, B.D., Rountree, E.S., Eisenhart, T.T., Dempsey, J.L., 2018. A practical beginner's guide to cyclic voltammetry. J. Chem. Educ. 95 (2), 197–206.

Gao, X., Zhang, Y., Wu, Q., Chen, H., Chen, Z., Lin, X., 2011. One step electrochemically deposited nanocomposite film of chitosan–carbon nanotubes–gold nanoparticles for carcinoembryonic antigen immunosensor application. Talanta 85 (4), 1980–1985.

Gutiérrez, A., Primo, E.N., Eguílaz, M., Parrado, C., Rubianes, M.D., Rivas, G.A., 2017. Quantification of neurotransmitters and metabolically related compounds at glassy carbon electrodes modified with bamboo-like carbon nanotubes dispersed in double stranded DNA. Microchem. J. 130, 40–46.

Hao, Y., Cui, Y., Qu, P., Sun, W., Liu, S., Zhang, Y., Li, D., Zhang, F., Xu, M., 2018. A novel strategy for the construction of photoelectrochemical sensing platform based on multifunctional photosensitizer. Electrochim. Acta 259, 179–187.

Hasanzadeh, M., Shadjou, N., Guardia, M.d.l., 2017. Current advancement in electrochemical analysis of neurotransmitters in biological fluids. Trac. Trends Anal. Chem. 86, 107–121.

Huang, B., Xiao, L., Dong, H., Zhang, X., Gan, W., Mahboob, S., Al-Ghanim, K.A., Yuan, Q., Li, Y., 2017. Electrochemical sensing platform based on molecularly imprinted polymer decorated N, S co-doped activated graphene for ultrasensitive and selective determination of cyclophosphamide. Talanta 164, 601–607.

Ilkhani, H., Hughes, T., Li, J., Zhong, C.J., Hepel, M., 2016. Nanostructured SERS-electrochemical biosensors for testing of anticancer drug interactions with DNA. Biosens. Bioelectron. 80, 257–264.

Kalwar, N.H., Tunesi, M.M., Soomro, R.A., Amir, M., Avci, A., Hallam, K.R., Kilislioglu, A., Karakus, S., 2017. Acetylsalicylic acid assisted hydrothermal growth of NiO, CuO and Co3O4 nanostructures and their application in the electro-catalytic determination of nalbuphine hydrochloride. J. Electroanal. Chem. 807, 137–144.

Li, X., Yuan, Y., Pan, X., Zhang, L., Gong, J., 2019. Boosted photoelectrochemical immunosensing of metronidazole in tablet using coral-like g-C3N4 nanoarchitectures. Biosens. Bioelectron. 123, 7–13.

Liu, B., Xie, Z., Liu, G., Gu, Y., Pan, S., Wang, H., 2018a. Elevated neuron-specific enolase and S100 calcium-binding protein B concentrations in cerebrospinal fluid of patients with anti-N-methyl-d-aspartate receptor encephalitis. Clin. Chim. Acta 480, 79–83.

Liu, C., Meng, F., Zhang, L., Zhang, D., Wei, S., Qi, K., Fan, J., Zhang, H., Cui, X., 1 March 2019. CuO/ZnO heterojunction nanoarrays for enhanced photoelectrochemical water oxidation. Appl. Surf. Sci. 469, 276–282.

Muoio, B., Pascale, M., Roggero, E., 2018. The role of serum neuron-specific enolase in patients with prostate cancer: a systematic review of the recent literature. Int. J. Biol. Mark. 33 (1), 10–21.

Niu, L.M., Lian, K.Q., Shi, H.M., Wu, Y.B., Kang, W.J., Bi, S.Y., 2013. Characterization of an ultrasensitive biosensor based on a nano-Au/DNA/nano-Au/poly(SFR) composite and its application in the simultaneous determination of dopamine, uric acid, guanine, and adenine. Sensor. Actuator. B Chem. 178, 10–18.

Pang, H., Zang, Y., Fan, J., Yun, J., Xue, H.G., 2018. Current advances in semiconductor nanomaterials-based photoelectrochemical biosensing. Chem. A Eur J.

Pussard, E., Chaouch, A., Said, T., 2014. Radioimmunoassay of free plasma metanephrines for the diagnosis of catecholamine-producing tumors. Clin. Chem. Lab. Med. 52 (3), 437–444.

Rubianes, M.a.D., Rivas, G.A., 2003. Carbon nanotubes paste electrode. Electrochem. Commun. 5 (8), 689–694.

Si, B., Song, E., 2018. Recent advances in the detection of neurotransmitters. Chemosensors 6 (1), 1.

Song, E., Yu, M., Wang, Y., Hu, W., Cheng, D., Swihart, M.T., Song, Y., 2015. Multi-color quantum dot-based fluorescence immunoassay array for simultaneous visual detection of multiple antibiotic residues in milk. Biosens. Bioelectron. 72, 320–325.

Soomro, R.A., 2017. Synthesis, Characterization and Application of Metal and Metal Oxide Nanostructures. GRIN Publishing.

Soomro, R.A., Tunesi, M.M., Karakus, S., Kalwar, N., 2017. Highly sensitive electrochemical determination of captopril using CuO modified ITO electrode: the effect of in situ grown nanostructures over signal sensitivity. RSC Adv. 7 (31), 19353–19362.

Tang, J., Han, L., Yu, Y., Kang, J., Zhang, Y., 2011. Studies of fluorescence immunosensor using eggshell membrane as immobilization matrix. J. Fluoresc. 21 (1), 339–346.

Tunesi, M.M., Kalwar, N., Abbas, M.W., Karakus, S., Soomro, R.A., Kilislioglu, A., Abro, M.I., Hallam, K.R., 2018. Functionalised CuO nanostructures for the detection of organophosphorus pesticides: a non-enzymatic inhibition approach coupled with nano-scale electrode engineering to improve electrode sensitivity. Sensor. Actuator. B Chem. 260, 480–489.

Tunesi, M.M., Soomro, R.A., Ozturk, R., 2016. CuO nanostructures for highly sensitive shape dependent electrocatalytic oxidation of N-acetyl-L-cysteine. J. Electroanal. Chem. 777, 40–47.

Tunesi, M.M., Soomro, R.A., Ozturk, R., 2017. The in situ growth of CuO nanostructures on an ITO substrate and its application as a highly sensitive electrode for the electrochemical determination of N-acetyl-L-cysteine. J. Mater. Chem. C 5 (10), 2708–2716.

Wang, H., Wang, Y., Zhang, Y., Wang, Q., Ren, X., Wu, D., Wei, Q., 2016. Photoelectrochemical immunosensor for detection of carcinoembryonic antigen based on 2D TiO 2 nanosheets and carboxylated graphitic carbon nitride. Sci. Rep. 6, 27385.

Wang, Q., Liu, Z., Zhang, S., Cui, Y., Gao, S., Wang, Y., 2019. Hydrothermal deposition of Cu2O-Ag nanoparticles co-sensitized TiO2 nanotube arrays and their enhanced photoelectrochemical performance. Separ. Purif. Technol. 211, 866–872.

Wu, T., Yan, T., Zhang, X., Feng, Y., Wei, D., Sun, M., Du, B., Wei, Q., 2018. A competitive photoelectrochemical immunosensor for the detection of diethylstilbestrol based on an Au/UiO-66 (NH2)/CdS matrix and a direct Z-scheme Melem/CdTe heterojunction as labels. Biosens. Bioelectron. 117, 575–582.

Xu, Y., Hun, X., Liu, F., Wen, X., Luo, X., 2015. Aptamer biosensor for dopamine based on a gold electrode modified with carbon nanoparticles and thionine labeled gold nanoparticles as probe. Microchimica Acta 182 (9–10), 1797–1802.

Yin, J., Guo, W., Qin, X., Zhao, J., Pei, M., Ding, F., 2017. A sensitive electrochemical aptasensor for highly specific detection of streptomycin based on the porous carbon nanorods and multifunctional graphene nanocomposites for signal amplification. Sensor. Actuator. B Chem. 241, 151–159.

Yu, T., Cheng, W., Li, Q., Luo, C., Yan, L., Zhang, D., Yin, Y., Ding, S., Ju, H., 2012. Electrochemical immunosensor for competitive detection of neuron specific enolase using functional carbon nanotubes and gold nanoprobe. Talanta 93, 433–438.

Yu, Y., Huang, Z., Zhou, Y., Zhang, L., Liu, A., Chen, W., Lin, J., Peng, H., 2019. Facile and highly sensitive photoelectrochemical biosensing platform based on hierarchical architectured polydopamine/tungsten oxide nanocomposite film. Biosens. Bioelectron. 126, 1–6.

Zhang, Y., Wang, M., Wang, Y., Feng, J., Zhang, Y., Sun, X., Du, B., Wei, Q., 2019. Label-free photoelectrochemical immunosensor for amyloid β-protein detection based on SnO2/CdCO3/CdS synthesized by one-pot method. Biosens. Bioelectron. 126, 23–29.

Zhu, G., Yin, X., Jin, D., Zhang, B., An, Y., Gu, Y., 2018. Paper based immunosensors: current trends in the types and applied detection techniques. Trac. Trends Anal. Chem.